Geometric Deformable Model Driven by CoCRFs: Application to Optical Coherence Tomography

Gabriel Tsechpenakis[1], Brandon Lujan[2], Oscar Martinez[1], Giovanni Gregori[2], and Philip J. Rosenfeld[2]

[1] Dept. of Electrical and Computer Engineering, University of Miami
gavriil@miami.edu,o.martinez4@umiami.edu
[2] Bascom Palmer Eye Institute, Miller School of Medicine, University of Miami
{BLujan,GGregori,prosenfeld}@med.miami.edu

Abstract. We present a geometric deformable model driven by dynamically updated probability fields. The shape is defined with the signed distance function, and the internal (smoothness) energy consists of a C^1 continuity constraint, a shape prior, and a term that forces the zero-level of the shape distance function towards a connected form. The image probability fields are estimated by our collaborative Conditional Random Field (CoCRF), which is updated during the evolution in an active learning manner: it infers class posteriors in pixels or regions with feature ambiguities by assessing the joint appearance of neighboring sites and using the classification confidence. We apply our method to Optical Coherence Tomography fundus images for the segmentation of geographic atrophies in dry age-related macular degeneration of the human eye.

1 Introduction

A challenging problem in computer and medical vision is to segment regions with boundary insufficiencies, i.e., missing edges and/or lack of texture contrast between regions of interest (ROIs) and background. In this paper we focus on two general categories of segmentation methods, namely the deformable models and the learning-based classification approaches.

Deformable models are divided into two main categories. The first class is the *parametric* or *explicit* deformable models [11,2,15,23], or active contours, which use parametric curves to represent the model shape. Edge-based parametric models use edges as image features, which usually makes them sensitive to noise, while region-based methods use region information to drive the curve [20,24,8]. A limitation of the latter methods is that they do not update the region statistics during the model evolution, and therefore local feature variations are difficult to be captured. Region updating is proposed in [3], where active contours with particle filtering is used for vascular segmentation.

Another class of deformable models is the *geometric* or *implicit* models [16,17,14], which use the level-set based shape representation, transforming the curves into higher dimensional scalar functions. In [16], the optimal function is the one that best fits the image data, it is piecewise smooth and presents discontinuities across the boundaries of different regions. In [17], a variational framework is proposed, integrating boundary

D. Metaxas et al. (Eds.): MICCAI 2008, Part I, LNCS 5241, pp. 883–891, 2008.

and region-based information in PDEs that are implemented using a level-set approach. These methods assume piecewise or Gaussian intensity distributions within each partitioned image region, which limits their ability to capture intensity inhomogeneities and complex intensity distributions. In [7], the Metamorphs was introduced, which updates a kernel-based approximation of the model interior texture during the evolution. The model dynamics are defined parametrically using Free Form Deformations, which sometimes is a limiting factor for capturing region details. Also, merging different curves on the image plane is formulated as detection of collision of different models, and therefore merging is not a property inherently defined in the model representation.

Learning-based region classification is also among the most popular approaches to medical image segmentation, with representative example the Markov Random Fields (MRFs) [6]. To obtain better probability smoothing, Conditional Random Fields (CRFs) were introduced in computer vision [13]. Although CRFs were first used to label sequential data, extensions of them are used for image segmentation [12,5,22]. The main advantage of CRFs is that they handle the known label bias problem [13], avoiding the conditional independence assumption among the features of neighboring sites. In [12] the Discriminative Random Fields (DRFs) are presented, which allow for computationally efficient MAP inference. Also, in [5], CRFs are used in different spatial scales to capture the dependencies between image regions of multiple sizes. A potential limitation of CRFs is that they do not provide robustness to unobserved or partially observed features, which is a common problem in most discriminative models.

Integrating deformable models with MAP inference methods is a recently introduced framework for propagating deformable models in a probabilistic manner, by formulating the *traditional* energy minimization as a MAP estimation problem. In the survey of [15], methods that use probabilistic formulations are described. In the work of [8] the integration of probabilistic active contours with MRFs in a graphical framework is proposed to overcome the limitations of edge-based probabilistic active contours. In [6], a framework that tightly couples 3D MRFs with deformable models is proposed for the 3D segmentation of medical images. Finally, to exploit the superiority of CRFs compared to common first-order MRFs, a coupling framework is proposed in [22], where a CRF and an implicit deformable model are integrated in a simple graphical model.

In this paper we present a probabilistic geometric deformable model that is driven by a *collaborative* CRF. The model evolution is solved as a joint MAP estimation problem for the model position and the image label field. In section 2, we define the model's shape and its internal energy, which consists of a C^1 continuity constraint, a shape prior, and a term that forces the zero-level of the shape distance function towards a connected form. The latter can be seen as a term that forces different closed curves on the image plane to merge, and therefore our model inherently carries the property of merging regions. During the evolution, described in 2.1, the model interior statistics are dynamically updated, and the new distributions are used in our CRF in an active learning manner. In section 3 we describe our *collaborative* CRF, which infers class posteriors in pixels and regions with feature ambiguities by assessing the joint appearance of neighboring sites and using classification confidence. In 4 we show our results on the segmentation of geographic atrophies in dry age-related macular degeneration of

the human eye, from Optical Coherence Tomography (OCT) fundus images. Finally, in 5 we give our conclusions.

2 Deformable Model

The model boundary $\mathcal{M}$ defines two regions in the image domain Ω, namely the region $\mathcal{R}_{\mathcal{M}}$ enclosed by the model $\mathcal{M}$ and the background $\Omega \backslash \mathcal{R}_{\mathcal{M}}$. The model shape $\Phi_{\mathcal{M}}$ is represented implicitly by its distance transform, as in [7,22]. The internal energy of the model consists of three individual terms, namely the smoothness constraint E_{smooth}, the distance from the target shape E_{shape}, and a partitioning energy E_{part},

$$E_{int}(\Phi_{\mathcal{M}}) = E_{smooth}(\Phi_{\mathcal{M}}) + E_{part}(\Phi_{\mathcal{M}}) + E_{shape}(\Phi_{\mathcal{M}}) \tag{1}$$

The smoothness term is defined as,

$$E_{smooth}(\Phi_{\mathcal{M}}) = \varepsilon_1 \mathcal{A}(\mathcal{R}_{\mathcal{M}}) + \varepsilon_2 \int \int_{\partial \mathcal{R}_{\mathcal{M}}} \|\nabla \Phi_{\mathcal{M}}(\mathbf{x})\| d\mathbf{x} \tag{2}$$

where ε_1 and ε_2 are weighting constants, $\partial \mathcal{R}_{\mathcal{M}}$ denotes a narrow band around the model boundary, and $\mathcal{A}(\mathcal{R}_{\mathcal{M}})$ denotes the area of the model interior. The minimization of this energy forces the model to the position with the minimum area enclosed and the maximum first-order smoothness along the model boundary; $\nabla \Phi_{\mathcal{M}}$ is defined $\forall \mathbf{x} \in \Omega$, and is used similarly as in the Mumford-Shah formulation [16].

The partitioning energy forces the regions $\Phi_{\mathcal{M}} \geq 0$ towards a connected form. It can be also seen as a term that minimizes the entropy of a set of particles, where the particles are assumed to be the connected components of $\Phi_{\mathcal{M}} \geq 0$, or equivalently the connected regions of $\mathcal{H}(\Phi_{\mathcal{M}})$. Let $\{\varphi_{\mathcal{M}}^{(i)}\}_{i=1}^{N} \subseteq \mathcal{H}(\Phi_{\mathcal{M}})$ be the set of N connected regions, and $e_{part}(\varphi_{\mathcal{M}}^{(i)})$ be the energy of each connected region $\varphi_{\mathcal{M}}^{(i)}$. We define this energy in terms of the distances between $\varphi_{\mathcal{M}}^{(i)}$ and the rest of the connected regions in the set $\mathcal{H}(\Phi_{\mathcal{M}})$,

$$e_{part}(\varphi_{\mathcal{M}}^{(i)}) = \sum_{j=1, j\neq i}^{N} \tilde{d}(\varphi_{\mathcal{M}}^{(j)}, \varphi_{\mathcal{M}}^{(i)}), \quad \tilde{d}(\varphi_{\mathcal{M}}^{(j)}, \varphi_{\mathcal{M}}^{(i)}) = \min_{\mathbf{x} \in \varphi_{\mathcal{M}}^{(j)}} \|\varphi_{\mathcal{M}}^{(i)} - \mathbf{x}\| \tag{3}$$

Then, the partitioning energy of the model is expressed as,

$$E_{part}(\Phi_{\mathcal{M}}) = \frac{1}{2} \sum_{i=1}^{N} e_{part}(\varphi_{\mathcal{M}}^{(i)}), \tag{4}$$

The minimization of this energy forces the model towards the minimum distances between the connected components of $\mathcal{H}(\Phi_{\mathcal{M}})$, i.e., forces different regions (curves) on the image plane to merge.

Finally, we define the shape energy term in a similar way as in [18,1], in terms of the distance between the model $\Phi_{\mathcal{M}}$ and the target shape $\Phi_{shape}(\mathbf{x})$: $\|\Phi_{\mathcal{M}}\mathcal{H}(\Phi_{\mathcal{M}}) - \Phi_{shape}\mathcal{H}(\Phi_{shape})\|$, where we include in the calculations only the regions of the model and target shape.

2.1 The Model Evolution

We formulate the deformable model evolution as a joint MAP estimation problem for the model position and the image label field,

$$\langle \Phi^*_{\mathcal{M}}, \mathcal{L}^* \rangle = \arg \max_{(\Phi_{\mathcal{M}}, \mathcal{L})} P(\Phi_{\mathcal{M}}, \mathcal{L}|F), \tag{5}$$

where $\mathcal{L}$ is the sites' (pixels or image patches) labels, i.e., $\mathcal{L} = \{-1, 1\}$, where -1 and 1 denote *background* and *model interior* respectively, and F is the observations set, i.e., the intensity distributions. For the posterior probability $P(\Phi_{\mathcal{M}}, \mathcal{L}|F)$, we adopt the decomposition of [22],

$$P(\Phi_{\mathcal{M}}, \mathcal{L}|F) \propto P(\Phi_{\mathcal{M}}) \cdot P(F) \cdot P(\mathcal{L}|\Phi_{\mathcal{M}}) \cdot P(\mathcal{L}|F), \tag{6}$$

where $P(\Phi_{\mathcal{M}})$ is the model prior, $P(\mathcal{L}|F)$ represents the pixel/region classification in a discriminative manner, and $P(\mathcal{L}|\Phi_{\mathcal{M}})$ is a likelihood term that introduces uncertainty between the classification and the deformable model position. The data prior $P(F)$ is calculated using the nonparametric intensity distribution of the model interior in every instance of the evolution process.

The model prior $P(\Phi_{\mathcal{M}})$ corresponds to the energy of eq. (1), and is defined in terms of the gibbs functional,

$$P(\Phi_{\mathcal{M}}) = (1/Z_{int}) \exp\{-E_{int}(\Phi_{\mathcal{M}})\}, \tag{7}$$

where the individual terms of $E_{int}(\Phi_{\mathcal{M}})$ are calculated using the definitions we described above; Z_{int} is a normalization constant. The maximization of this prior forces the model towards a position with the minimum enclosed area and maximum smoothness along the boundary, with the smallest distance to the target shape, and the minimum *entropy* as defined in eqs. (3)-(4).

We define the likelihood $P(\mathcal{L}|\Phi_{\mathcal{M}})$ as the softmax function,

$$P(l_i|\Phi_{\mathcal{M}}) = \frac{1}{1 + \exp\{-\Phi_{\mathcal{M}}(\mathbf{x}_i)\}}, \tag{8}$$

where $l_i = \{-1, 1\}$ is the label of the i-th pixel or region $\mathbf{x}_i$. This term indicates that the probability of a site belonging to the model interior rapidly increases as $\Phi_{\mathcal{M}}(\mathbf{x}) > 0$ increases, and converges to zero as $\Phi_{\mathcal{M}}(\mathbf{x}) < 0$ decreases; also $P(l_i|\Phi_{\mathcal{M}}) = 0.5$ $\forall \mathbf{x}_i \in \Omega : \Phi_{\mathcal{M}}(\mathbf{x}_i) = 0$. Also, if $\mathbf{x}_i$ is a region, we consider its center to estimate this probability.

The remaining term $P(\mathcal{L}|F)$ in eq. (6) is calculated using our CRF framework described below.

3 The Collaborative CRF

We use a Conditional Random Field (CRF) formulation to calculate the probability field $P(\mathcal{L}|F)$ that drives the deformable model evolution, according to eqs. (5) and (6). We implement interactions that enforce similar class labels (*model interior* or *background*)

between all sites containing similar intensity distributions; these interactions are driven by the classification confidence to assist weakly labeled sites. To improve classification in cases of region ambiguities, we also use correlative information between neighboring sites, by estimating their joint intensity distributions.

Let $F = \{f_i\}_{i \in \mathcal{S}}$, where f_i is the intensity distribution from a site i, and $\mathcal{S}$ is the set of all sites. Also, let $\mathcal{L} = \{l_i\}_{i \in \mathcal{S}}$ be the set of corresponding labels for all sites in $\mathcal{S}$, with $l_i = \{-1, 1\}$ (background, ROI). If N_i denotes the spatial neighborhood of each site i, we can then say that conditioned on the discrete observations F, the distribution over the labels $p(\mathcal{L}|F)$ can be written as a first order CRF of the form,
$p(\mathcal{L}|F) =$

$$\frac{1}{z} \exp\left\{ \sum_{i \in \mathcal{S}} \mathbf{A}(l_i, f_i) + \sum_{i \in \mathcal{S}} \sum_{j \in N_i} \left[\mathbf{I}(l_i, l_j, f_i, f_j, K_i, K_j) + \mathbf{C}(l_i, l_j, f_{ij}) \right] \right\}, \quad (9)$$

where z is a normalization constant.

The unary *association potential* $\mathbf{A}(y_i, x_i)$ is estimated using a discriminative classifier (Support Vector Machine) to directly calculate the class posterior as mapping between the distribution f_i and the class l_i [12],

$$\mathbf{A}(l_i, f_i) = \log P(l_i|f_i), \quad (10)$$

The *interaction potential* $\mathbf{I}(l_i, l_j, f_i, f_j, K_i, K_j)$ compares the intensity distributions f_i and f_j and enhances classification by forcing smoothness between the neighboring l_i and l_j,

$$\mathbf{I}(l_i, l_j, f_i, f_j, K_i, K_j) = \frac{1}{z_{int}} \exp\left\{ \frac{\delta(l_i - l_j)}{\sigma^2} \right\} \beta(f_i, f_j) \gamma(K_i, K_j) \quad (11)$$

where z_{int} is a normalizing constant, $\delta(l_i - l_j) = 0$ if $l_i \neq l_j$, and $\delta(l_i - l_j) = 1$ if $l_i = l_j$, σ^2 controls the smoothing, and $\beta(f_i, f_j)$ measures the distance between i and j in the feature space; here we use the Bhattachayya distance for measuring the distributions similarity. We modulate the role of the interaction potential by the relative classification confidence $\gamma(K_i, K_j)$ of the sites i and j; K_i and K_j are the corresponding confidences representing how strong the discriminative classification of each site is. As a measure of confidence we use the distance from the classification boundary, although more efficient measures can be found in the literature [10]. To measure the relative confidence between two neighboring sites, we use the pairwise softmax function,

$$\gamma(K_i, K_j) = \frac{1}{1 + \exp\{\alpha(K_i - K_j)\}}, \ \alpha > 0, \quad (12)$$

where K_i and K_j are the classification confidence values for the sites i and j respectively, and α is a constant regulating the confidence similarity. The value of $\gamma(K_i, K_j)$ is only dependent on the relative value of K_i with respect to K_j: $K_i \gg K_j \Leftrightarrow \gamma \to 0$ and $K_i \ll K_j \Leftrightarrow \gamma \to 1$. This weighing function allows the interaction in eq. (11) between i and j only if site j is more confidently classified than site i. This guarantees that interaction will generally *flow* from sites labeled with relative confidence to sites labeled with relative uncertainty.

The *correlative potential* $\mathbf{C}(l_i, l_j, f_{ij})$ is used to improve classification in instances of region ambiguities by evaluating neighboring sites that could be portraying a single region,

$$\mathbf{C}(l_i, l_j, f_{ij}) = \log P(l_i = l_j | f_{ij}), \tag{13}$$

where f_{ij} is the joint intensity distribution of the sites i and j. To consider the joint appearance of two sites, we evaluate whether they are complimentary to each other with respect to their classification confidence: f_i and f_j are complimentary if $\{j \in N_i : K_i, K_j \leq K_{ij}\}$, where K_{ij} is the classification confidence for the joint distribution f_{ij}. In other words the classifier treats neighboring sites as possible regions of the same class that have erroneously been segmented apart, and decides whether or not they belong to the same class. Note that here, as confidence measurement we use the same classification probabilities (using the distance from the decision boundaries [19]); currently we are working towards generalizing this confidence-driven approach using the *belief* and *plausibility* terms from the Dempster-Shafer evidence theory.

4 Segmentation of Geographic Atrophy in the Retina

Age-related Macular Degeneration (AMD) has become the most common cause of severe irreversible vision loss in developed countries. In patients with advanced dry AMD, most of the severe vision loss results from atrophy of the retinal pigment epithelium (RPE). Confluent areas of RPE atrophy are clinically referred to as **geographic atrophy (GA)**, which can cause legal blindness if it affects the central macula. GA is currently present in 3.5% of all people 75 years and older in the United States [21], and this number is expected to double by 2020 [4]. There is currently no effective treatment for GA and there is only a rudimentary understanding of its pathophysiology. Furthermore, its visibility by standard photography depends on the degree of pigmentation present in the surrounding intact RPE. A new imaging modality, ***Spectral Domain Optical Coherence Tomography (SDOCT)***, demarcates areas of GA precisely even when it cannot be identified by photography. It utilizes the principles of reflectometry and interferometry to obtain structural information from the retina and layers under the retina at different depths along each axial scan (A-scan). One commercially available model, the Cirrus HD OCT (Carl Zeiss Meditec, Dublin, CA) images a $6mm \times 6mm \times 2mm$ volume of the central macula at a rate of $27,000$ A-scans/sec. It utilizes a broadband superluminescent diode with a wavelength centered at $840nm$. This provides an axial resolution of $5\mu m$ and a lateral resolution of $20\mu m$. SDOCT can be reconstructed to generate an $enface$ SDOCT image, allowing for precise topographic localization of GA [9].

We used our method to automatically segment GA from *en face* SDOCT images. In both examples we present here, we used a circle as target shape. **Fig. 1** illustrates our results using a set of A-scans, where the brighter region is the GA: the three images were obtained using the intensity values (a) in a predefined depth across the A-scans, (b) of all depths from each scan (with averaging), and (c) a specific depth range from each scan (bounded by the so-called *anatomic countour*); the latter is the fundus image used for patient evaluation. We illustrate these three cases to show the performance of our approach on the same data and under different rates of region ambiguities. In Fig. 1(d) and (e) we illustrate the model evolution on the image of Fig. 1(c), using one

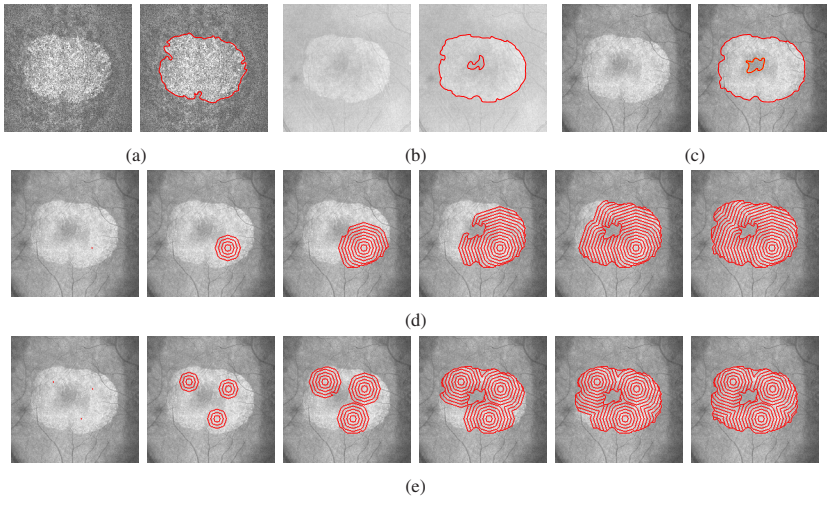

Fig. 1. GA segmentation in SDOCT fundus images: (a)-(c) images obtained using intensities from different depths across the A-scans; (d)-(e): model evolution using one and three markers for the model initialization. The model boundaries are shown in red.

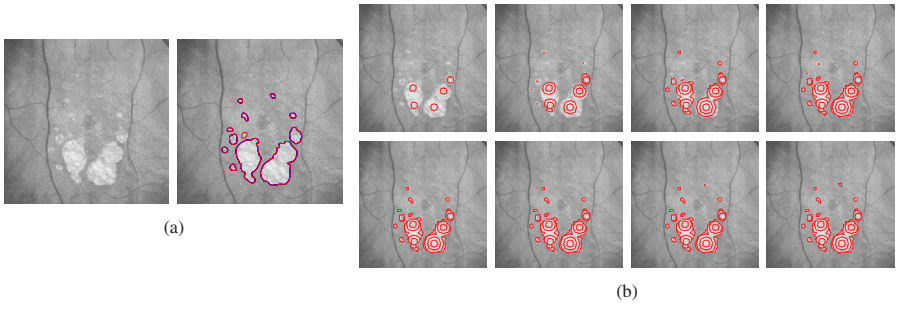

Fig. 2. GA segmentation: our dynamically updated CoCRF detects new GA regions during the model evolution. The model boundaries are shown in red.

and three markers for initialization respectively. The image resolution is 200×200 pixels, and in our CoCRF we used 5×5 patches as sites. **Fig. 2** illustrates another example of GA segmentation: (a) the original image (left) and the segmentation result (right); (b) the model evolution using five markers for initialization. During the evolution, new regions are detected by our CoCRF, due to the dynamic updating of the model interior statistics, and the confidence-driven classification. In this case, the CoCRF probability field overcomes the effect of the partitioning energy term of eqs. (3)-(4), which forces the zero-level of the model distance function towards a connected form. In this example we used pixels as sites in our CoCRF.

For the numerical validation of our method's performance, we used 15 subjects (A-scan sets), from which we manually selected a depth value and a depth range (inside the anatomic contour) to produce the fundus images similar to Fig. 1(a), (c). We

Table 1. Segmentation results for the fifteen subjects (see text). Image size $= 200 \times 200$ pixels.

Subject	♯1	♯2	♯3	♯4	♯5	♯6	♯7	♯8	♯9	♯10	♯11	♯12	♯13	♯14	♯15
Ground-truth	12871	10347	9305	7127	4955	4553	4432	4201	3019	2978	2121	1763	1229	1109	931
True positives (pixels)	12839	10318	9285	7113	4945	4542	4420	4192	3014	2974	2117	1758	1225	1106	928
False positives (pixels)	23	32	21	11	13	12	16	9	14	6	8	12	7	11	8

compared our segmentation results with the detailed manual segmentation that two experts from Bascom Palmer Eye Institute ($www.bpei.med.miami.edu$, University of Miami) performed as part of their clinical practice. We recorded the ratio $\frac{\mathcal{A}(\mathcal{R}_m \bigcap \mathcal{R}_a)}{\mathcal{A}(\mathcal{R}_m)}$, where $\mathcal{R}_m$, $\mathcal{R}_a$ denote the manually and automatically estimated regions, and $\mathcal{A}(\cdot)$ denotes the area. The ratio variations for the three kinds of fundus images were: (i) single A-scan depth: $98.6 - 99.3\%$, (ii) entire A-scan depth range: $98.9 - 99.7\%$, and (iii) anatomic contour-determined A-scan depth range: $99.7 - 99.8\%$. Table 1 illustrates the validation results for the examined data set, where the fundus images are 200×200 pixels: the false positives (background regions that were detected as GA) are mainly due to small brighter background regions outside the main (bigger) GA segments. Currently we are using our method in clinical trials for further validation.

5 Conclusions

We presented a deformable model integrated with discriminative learning-based classification, with the model interior statistics being dynamically updated and used in an active learning manner. For the classification, we used a new CRF-based collaborative framework (CoCRF), which infers class posteriors in regions with intensity ambiguities, by using the joint appearance and the classification confidence of neighboring sites. We demonstrated our results on the segmentation of geographic atrophies in dry age-related macular degeneration of the human eye, from SDOCT fundus images.

References

1. Chan, T., Zhu, W.: Level Set Based Shape Prior Segmentation. In: CVPR (2005)
2. Cohen, L.D., Cohen, I.: Finite-element Methods for Active Contour Models and Balloons for 2-D and 3-D Images. IEEE PAMI 15, 1131–1147 (1993)
3. Florin, C., Williams, J., Paragios, N.: Globally Optimal Active Contours, Sequential Monte Carlo and On-line Learning for Vessel Segmentation. In: ECCV (2006)
4. Friedman, D.S., O'Colmain, B.J., Muñoz, B., Tomany, S.C., McCarty, C., de Jong, P.T., Nemesure, B., Mitchell, P., Kempen, J.: Prevalence of age-related macular degeneration in the United States. Arch. Ophthalmol. 122(4), 564–572 (2004)
5. He, X., Zemel, R., Carreira-Perpinan, M.: Multiscale Conditional Random Fields for Image Labeling. In: CVPR (2004)
6. Huang, R., Pavlovic, V., Metaxas, D.: A Tightly Coupled Region-Shape Framework for 3D Medical Image Segmentation. In: ISBI (2006)
7. Huang, X., Metaxas, D., Chen, T.: Metamorphs: Deformable Shape and Texture Models. In: CVPR (2004)

8. Huang, R., Pavlovic, V., Metaxas, D.: A Graphical Model Framework for Coupling MRFs and Deformable Models. In: CVPR (2004)
9. Jiao, S., Knighton, R., Huang, X., Gregori, G., Puliafito, C.: Simultaneous acquisition of sectional and fundus ophthalmic images with spectral-domain optical coherence tomography. Optics Express 13(2), 444–452 (2005)
10. Kapoor, A., Grauman, K., Urtasun, R., Darrell, T.: Active Learning with Gaussian Processes for Object Categorization. In: ICCV (2007)
11. Kass, M., Witkin, A., Terzopoulos, D.: Snakes: Active contour models. Int'l. Journal of Computer Vision 1, 321–331 (1987)
12. Kumar, S., Hebert, M.: Discriminative Fields for Modeling Spatial Dependencies in Natural Images. Advances in Neural Information Processing Systems (2004)
13. Lafferty, J., McCallum, A., Pereira, F.: Conditional Random Fields: Probabilistic Models for Segmenting and Labeling Sequence Data. In: ICML (2001)
14. Malladi, R., Sethian, J., Vemuri, B.: Shape Modeling with Front Propagation: A Level Set Approach. IEEE PAMI 17(2), 158–175 (1995)
15. McInerney, T., Terzopoulos, D.: Deformable Models in Medical Image Analysis: A Survey. Medical Image Analysis 1(2) (1996)
16. Mumford, D., Shah, J.: Optimal Approximations by Piecewise Smooth Functions and Associated Variational Problems. Communications on Pure and Applied Mathematics 42(5), 577–685 (1989)
17. Paragios, N., Deriche, R.: Geodesic Active Regions and Level Set Methods for Supervised Texture Segmentation. Int'l Journal of Computer Vision 46(3), 223–247 (2002)
18. Paragios, N., Rousson, M., Ramesh, V.: Matching Distance Functions: A Shape-to-Area Variational Approach for Global-to-Local Registration. In: Heyden, A., Sparr, G., Nielsen, M., Johansen, P. (eds.) ECCV 2002. LNCS, vol. 2351, pp. 775–789. Springer, Heidelberg (2002)
19. Platt, J.C.: Probabilistic outputs for support vector machines and comparisons to regularized likelihood methods. In: Advances in Large Margin Classifiers, pp. 61–74. MIT Press, Cambridge (1999)
20. Ronfard, R.: Region-based strategies for active contour models. Int'l Journal of Computer Vision 13(2), 229–251 (1994)
21. Smith, W., Assink, J., Klein, R., Mitchell, P., Klaver, C.C., Klein, B.E., Hofman, A., Jensen, S., Wang, J.J., de Jong, P.T.: Risk factors for age-related macular degeneration: Pooled findings from three continents. Ophthalmology 108(4), 697–704 (2001)
22. Tsechpenakis, G., Metaxas, D.: CRF-driven Implicit Deformable Model. In: CVPR (2007)
23. Xu, C., Prince, J.L.: Snakes, Shapes and Gradient Vector Flow. IEEE Trans. on Image Processing 7(3), 359–369 (1998)
24. Zhu, S., Yuille, A.: Region Competition: Unifying snakes, region growing, and Bayes/MDL for multi-band image segmentation. IEEE PAMI 18(9), 884–900 (1996)